Biomaterials 330 (2026) 124010

Contents lists available at ScienceDirect

Biomaterials

journal homepage: www.elsevier.com/locate/biomaterials

FAK modulates immune response and fibroblast activation in biomaterial-induced fibrosis

Marc A. Fernández-Yagüe [a,b,c], Graham F. Barber [a,b], Aránzazu del Campo [d,e], Andrés J. García [a,b,*]

[a] Petit Institute for Bioengineering and Bioscience, Georgia Institute of Technology, Atlanta, GA, USA
[b] Woodruff School of Mechanical Engineering, Georgia Institute of Technology, Atlanta, GA, USA
[c] Department of Chemistry, Queen Mary University of London, London, UK
[d] INM – Leibniz Institute for New Materials, Saarbrücken, Germany
[e] Saarland University, Chemistry Department, Saarbrücken, Germany

ARTICLE INFO

Keywords:
PEG-Norbornene
Fibrotic capsule
Myofibroblast activation
Immune modulation
Foreign body response
Cytokine profiling
Subcutaneous implant model
Stromal and immune cell modulation

ABSTRACT

Fibrotic capsule formation remains a major barrier in the clinical performance of biomedical implants. Here, we demonstrate that synthetic hydrogels mimicking the mechanical properties of fibrotic tissue trigger stromal cell activation and immune remodeling via focal adhesion kinase (FAK)-mediated mechanotransduction. Using a mechanically tunable poly(ethylene glycol) hydrogel platform and subcutaneous implantation in mice, we show that pharmacological inhibition of FAK activity significantly reduces α-smooth muscle actin (α-SMA)-positive myofibroblast activation, collagen I deposition, and fibrotic capsule thickness in a hydrogel stiffness-dependent manner. Flow cytometry and cytokine profiling revealed that FAK inhibition alters the fibrotic niche by reducing CD163-positive M2c macrophages and significantly downregulating pro-fibrotic cytokines including IL-6, and VEGF, while transiently increasing regulatory T cells and elevating IL-10 levels. Importantly, these changes occurred without parallel increases in canonical pro-inflammatory cytokines, indicating selective modulation rather than global immune suppression or activation. These findings position FAK as a central hub translating mechanical cues into coordinated stromal and immune responses. Targeting FAK mechanotransduction may provide a therapeutic strategy to mitigate foreign body responses and improve implant integration across regenerative applications.

1. Introduction

Biomaterial implants are widely used in clinical practice, yet their long-term performance is often compromised by chronic inflammation and fibrotic capsule formation [1–4]. Recent advances in bioactive and immunocompatible hydrogel systems have highlighted opportunities to mitigate these responses while supporting host integration [5,6]. This host response is coordinated by complex interactions between immune and stromal cells that dynamically respond to the mechanical and biochemical cues present at the material–tissue interface. Whereas the cellular and molecular composition of the fibrotic response has been extensively studied, the upstream biophysical cues and immunological microenvironment that initiate fibroblast activation remain poorly understood. Among these biophysical cues, matrix stiffness has emerged as a critical determinant of fibrotic remodeling. Materials with elastic moduli exceeding ~15 kPa promote α-smooth muscle actin (α-SMA) expression in myofibroblasts and drive extracellular matrix (ECM) deposition. In contrast, compliant materials (<1 kPa) rarely induce sustained fibroblast contractility or fibrotic encapsulation. These stiffness ranges mirror those measured in fibrotic tissues such as early hypertrophic scars (~5–15 kPa), idiopathic pulmonary fibrosis (~5–20 kPa), and evolving liver fibrosis, highlighting their clinical relevance [7,8].

Focal adhesion kinase (FAK) is a mechanosensitive tyrosine kinase that plays a central role in translating extracellular matrix signals into intracellular responses. Structurally, FAK comprises a FERM domain that regulates its autoinhibition and membrane localization, a central kinase domain responsible for its catalytic activity, and a C-terminal focal adhesion targeting domain that anchors it to integrin-based adhesion complexes [9,10]. Upon integrin engagement and

* Corresponding author. Petit Institute for Bioengineering and Bioscience, Georgia Institute of Technology, Atlanta, GA, USA.
E-mail address: andres.garcia@me.gatech.edu (A.J. García).

https://doi.org/10.1016/j.biomaterials.2026.124010
Received 22 December 2025; Accepted 18 January 2026
Available online 19 January 2026

mechanical loading, FAK undergoes autophosphorylation at tyrosine 397 (Y397), creating a high-affinity binding site for Src-family kinases. This leads to full activation of FAK and downstream phosphorylation cascades regulating cytoskeletal tension, cell survival, and differentiation. In fibrotic contexts, persistent FAK activation sustains myofibroblast phenotypes and ECM remodeling, making it a key node in the fibrotic signaling network [11,12]. FAK activation is highly dependent on substrate stiffness. While basal activity remains low on soft matrices mimicking healthy tissue (~0.5–5 kPa), phosphorylation increases markedly on stiffer substrates, with significant activation typically observed above 8–10 kPa and plateauing beyond 15–20 kPa [13–15]. This defines a mechanosensitive threshold above which integrin-mediated mechanical inputs consistently engage FAK-dependent signaling. In our prior work, we confirmed this transition zone by measuring FAK phosphorylation in fibroblasts cultured on substrates ranging from 1 to 30 kPa, observing robust Y397 activation above 8 kPa, with levels stabilizing at 15 kPa [8]. This threshold defines a stiffness threshold beyond which mechanical inputs consistently engage FAK-mediated adhesion signaling [16]. Building on this finding, we demonstrated that the choice of adhesive motif influences the immune microenvironment, as RGD-presenting PEG hydrogels recruit distinct macrophage subpopulations and alter cytokine signatures compared to scrambled RDG controls [17].

In addition to its well-established role in fibroblast activation, FAK functions as an immunomodulatory kinase. Nuclear FAK drives the transcription of chemokines that recruit regulatory T cells (Tregs), promoting immune suppression in various pathologies, including cancer [18]. Furthermore, FAK regulates myeloid cell adhesion, survival, and inflammatory activation [19,20]. Pharmacological FAK inhibition has been shown to reduce Treg and M2-like tumor-associated macrophage populations, enhance $CD8^+$ T cell infiltration, and synergize with immune checkpoint blockade [18,21]. However, the role of FAK in modulating immune responses within fibrotic encapsulation remains underexplored, particularly in the context of fibrotic responses to biomaterials. Here, using a tunable synthetic hydrogel platform to replicate the mechanical stiffness characteristic of fibrotic tissues, we evaluated the effects of implant stiffness on stromal and immune cell responses *in vivo*. Hydrogels were functionalized with RGD to provide controlled integrin-mediated adhesion, a design we previously showed reshapes macrophage composition relative to RDG [17], and consistent with a large body of literature using RGD-presenting hydrogels. Our findings reveal a stiffness-dependent fibrotic program and identify FAK inhibition as a promising strategy to attenuate mechanosensitive remodeling and immune infiltration at the tissue-biomaterial interface.

2. Results

2.1. FAKi attenuates peri-implant capsule formation and limits myofibroblast activation and collagen deposition

Mechanical stiffness and FAK-mediated mechanotransduction are determinant factors driving host responses and myofibroblast activation [7,22,23]. To investigate the effects of hydrogel stiffness on fibrotic cell responses through FAK signaling, we used a hydrogel platform with tunable mechanical properties. Hydrogels composed of four-arm polyethylene glycol-norbornene (PEG-4aNB) were crosslinked via dithiothreitol (DTT) and functionalized with integrin-binding RGD peptide to promote cellular adhesion (Fig. 1A). Following photopolymerization using lithium phenyl-2,4,6-trimethylbenzoylphosphinate (LAP) as photoinitiator under UV irradiation, mechanically defined hydrogel disks

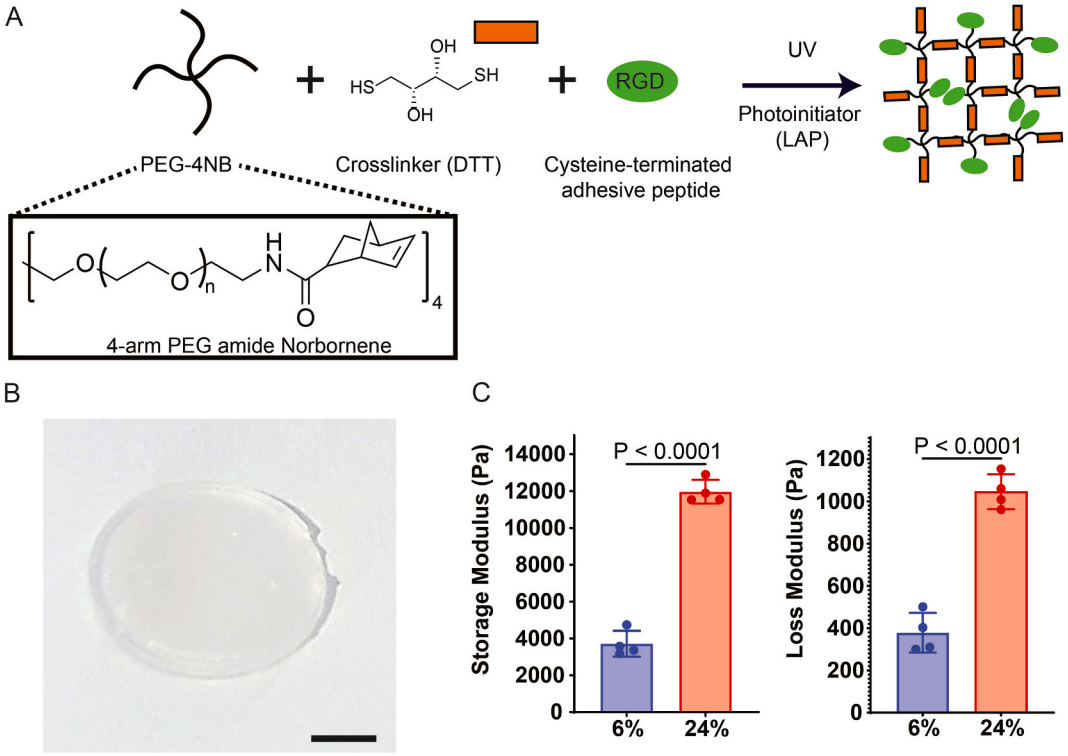

Fig. 1. PEG-4aNB hydrogels and mechanical characterization. A) Four-arm PEG-norbornene (PEG-4aNB) macromer (2 kDa) was photo-cross-linked with dithiothreitol (DTT) in the presence of the photoinitiator LAP; an RGD peptide was incorporated for cell adhesion. UV exposure (85 mW cm^{-2}, 10 s) yielded covalently cross-linked disks. **B)** Representative hydrogel used for subcutaneous implantation (scale bar = 5 mm). Both 6 % and 24 % (w/v) RGD–PEG-4aNB hydrogels were cast as 10 mm diameter × 2 mm thick discs (PEG-4aNB 2 kDa; DTT stoichiometric; RGD 1 mM). **C)** Storage modulus (G′) and loss modulus (G″) of soft and stiff hydrogels measured by time-sweep rheology (1 Hz, 1.5 % strain, 25 °C). Soft hydrogels (6 % w/v PEG-4aNB, storage modulus ≈ 4 kPa) and stiff hydrogels (24 % w/v PEG-4aNB, storage modulus ≈ 12 kPa) are shown (mean ± SD from independently prepared batches, n = 4 per group). P-values calculated using unpaired two-tailed t-tests.

(10 mm diameter, 2 mm thick) suitable for subcutaneous implantation were generated (Fig. 1B). Rheological measurements confirmed predominantly elastic behavior (storage modulus G′ significantly higher than loss modulus G″), indicating robust gel networks (Fig. 1C). The measured storage and loss moduli closely matched theoretical predictions, yielding soft (G' = 3900 ± 590 Pa) and stiff (G' = 12,100 ± 520 Pa) hydrogels, and these gels were reproducible across independently prepared hydrogel batches. These values are physiologically relevant and closely match stiffness values found in early fibrotic scars (~5–15 kPa) [24].

To examine the impact of FAK signaling on fibrotic capsule development, mice received one soft (4 kPa) and one stiff (12 kPa) hydrogel in the dorsal flank, positioned within the thin fascia layer, separating the panniculus carnosus from underlying fat tissue. The implants were placed in separate subcutaneous pockets on each side of the dorsum to avoid inter-implant interactions. Mice were administered twice-daily subcutaneous injections of the FAK catalytic inhibitor VS-6063 (15 μM, twice daily) or vehicle control (DMSO) on days 0–10 post-implantation and explant analyses performed at days 14 and 35 (Fig. 2A).

At 14- or 35-days post-implantation, samples were excised and processed for histological analyses, including Masson's trichrome staining to assess cellular infiltration and evaluate extracellular matrix (ECM) deposition (Fig. 2B). To evaluate fibrotic capsule maturation over time, peri-implant tissue sections were analyzed morphometrically on the side facing the panniculus carnosus (toward the skin), designated as the 'superior' side, while the opposing surface facing the fat pad and internal fascia was termed the 'inferior' side (Fig. 2B). To avoid anatomical variability at the implant–fat pad interface, all morphometric analyses were conducted on the 'superior' capsule wall, which forms adjacent to the panniculus carnosus. This region exhibited more consistent fibrotic progression and was less affected by surgical disruption or residual fascia, making it a reliable anatomical plane for assessing fibrosis progression and therapeutic response.

For stiff hydrogels, fibrotic capsule thickness, α-SMA expression, and collagen I deposition all increased from day 14 to day 35 in vehicle-treated mice. Capsule thickness nearly doubled from 43.6 ± 6.1 μm to 79.4 ± 17.8 μm (Fig. 2C and D), indicating progressive fibrotic remodeling. This was accompanied by significant increases in myofibroblast activation and matrix deposition, as shown by elevated α-SMA density ($P = 0.0389$; Fig. 2E and F) and collagen I accumulation ($P = 0.0280$; Fig. 2G and H). FAK inhibition (FAKi) did not significantly affect capsule thickness at day 14 (31.6 ± 18.3 μm, $P = 0.1773$), but by day 35, it reduced capsule thickness by 32 % compared to vehicle controls (53.6 ± 17.6 μm, $P = 0.0044$). Moreover, FAKi treatment significantly blunted the fibrotic trajectory, reducing α-SMA density by 51 % ($P = 0.0210$) and collagen I levels by 42 % ($P = 0.0423$) at day 35. In stark contrast to stiff hydrogels, soft hydrogels (4 kPa) exhibited minimal fibrotic responses (capsule thickness, α-SMA, and collagen I staining) irrespective of FAK inhibitor administration (Fig. S1). This mechanical threshold effect confirms that fibrotic capsule formation requires specific mechanical stimuli, consistent with previously reported stiffness-dependent mechanisms of fibrosis [25]. Because of the strong fibrotic responses to stiff hydrogels compared to soft hydrogels, subsequent analyses focused on responses to stiff hydrogels.

2.2. FAK inhibition suppresses YAP–myofibroblast coupling in stiff hydrogel capsules

To assess whether the attenuated capsule phenotype under FAK inhibition was accompanied by reduced mechanical signaling, we immunostained day 35 capsules from stiff (12 kPa) implants for phosphorylated FAK (pFAK-Y397) and α-SMA (Fig. 3A and B). Vehicle-treated capsules exhibited robust pFAK-Y397 signal within the capsule wall together with strong α-SMA staining (Fig. 3A). In contrast, FAKi-treated capsules showed markedly reduced pFAK-Y397 staining accompanied by reduced α-SMA signal (Fig. 3A). Higher-magnification images highlighted co-localization of YAP nuclear signal within α-SMA$^+$ cells in vehicle-treated capsules, whereas YAP signal within α-SMA$^+$ cells was reduced under FAKi (Fig. 3B).

Quantification confirmed a strong reduction in α-SMA staining within the capsule ($P = 0.0004$; Fig. 3C) and a significant reduction in pFAK-Y397 signal with FAKi ($P < 0.0001$; Fig. 3D) compared to vehicle controls. Importantly, we quantified YAP nuclear localization within the activated myofibroblast compartment. The percentage of α-SMA$^+$ cells that were also nuclear YAP$^+$ was reduced by more than two-fold in FAKi-treated capsules compared to vehicle controls ($P < 0.0001$; Fig. 3E). Together, these data show that pharmacological inhibition of FAK reduces focal adhesion signaling *in vivo* and disrupts YAP nuclear localization within α-SMA$^+$ cells, consistent with suppression of a stiffness-driven mechanotransduction program within fibrotic capsules.

To examine how fibroblast subtypes evolve over time during fibrotic capsule formation, we used spectral flow cytometry and a gating strategy to identify lineage-negative (CD45$^-$CD11b$^-$CD31$^-$TER119$^-$EpCAM$^-$) fibroblasts based on the expression of collagen I (Col I), CD26 (DPP4), and α-smooth muscle actin (α-SMA) (Fig. 4A). These markers delineate Engrailed-1 (En1) lineage-like fibroblast subsets implicated in fibrosis and wound repair. En1$^+$ fibroblasts (Col I$^+$ DPP4$^+$ α-SMA$^+$) are contractile and pro-fibrotic, whereas En1$^-$ fibroblasts (Col I$^+$ DPP4$^-$ α-SMA$^-$) lack myogenic differentiation and are associated with regenerative ECM remodeling [26]. From day 14 to day 35, α-SMA$^+$ En1$^+$ myofibroblasts increased for both FAKi- and vehicle-treated mice (Fig. 4B), consistent with progressive matrix stiffening and capsule maturation, whereas En1$^-$ fibroblasts declined (Fig. 4C). At day 35, FAKi reduced the frequency of En1$^+$ fibroblasts by nearly 30 % compared to vehicle ($P = 0.0153$; Fig. 4B), whereas En1$^-$ fibroblasts increased to over 60 % of the lineage-negative population ($P = 0.0040$; Fig. 4C). These results demonstrate that inhibition of FAK kinase activity regulates lineage-specific fibroblast dynamics at the tissue-biomaterial interface, suppressing the accumulation of pro-fibrotic, contractile fibroblasts while promoting maintenance of reparative subsets.

2.3. FAKi alters immune cell composition in the capsule and suppresses pro-fibrotic cytokine networks

Because of the established roles of inflammation in fibrosis progression and the known influence of FAK signaling on immune cell function and cytokine expression [27–29], we next examined whether pharmacological inhibition of FAK alters immune cell composition within the fibrotic capsule. We performed multiparametric flow cytometry on cells recovered from tissue capsules harvested at days 14 and 35 post-implantation, utilizing a panel of lymphoid and myeloid cell markers implicated in fibrosis and biomaterial responses.

Lymphoid (CD45$^+$CD11b$^-$) and myeloid (CD45$^+$CD11b$^+$) compartments were defined via bivariate plot gating (Fig. 5A). In the lymphoid compartment, CD4$^+$ T cell numbers remained stable between day 14 and 35 and were unaffected by FAKi, indicating minimal influence of FAK on helper T cell numbers (Fig. 5B). In contrast, regulatory T cells (Tregs; CD25$^+$FoxP3$^+$) were higher in FAKi-treated mice than with vehicle and remained at similar levels from day 14 to day 35 (Fig. 5C), indicating a sustained immunosuppressive response.

Given the central role of myeloid cells in orchestrating fibrosis and foreign body responses [27,30,31] and the involvement of FAK signaling in myeloid adhesion, motility, and activation [19,20,29], we next characterized capsule-resident myeloid subsets based on differential surface expression of Siglec-F, Ly6G, Ly6C, and F4/80, enabling resolution of eosinophils (Siglec-F$^+$), neutrophils (Ly6G$^+$), classical (Ly6C$^+$) and non-classical (Ly6C$^-$) monocytes, and macrophages (F4/80$^+$). Among these populations, non-classical (Ly6C$^-$) monocytes were higher at day 14 in FAKi-treated mice than in vehicle controls ($P = 0.0489$; Fig. 5D). However, their frequency declined from day 14 to day 35 in both groups, indicating a consistent time-dependent decrease

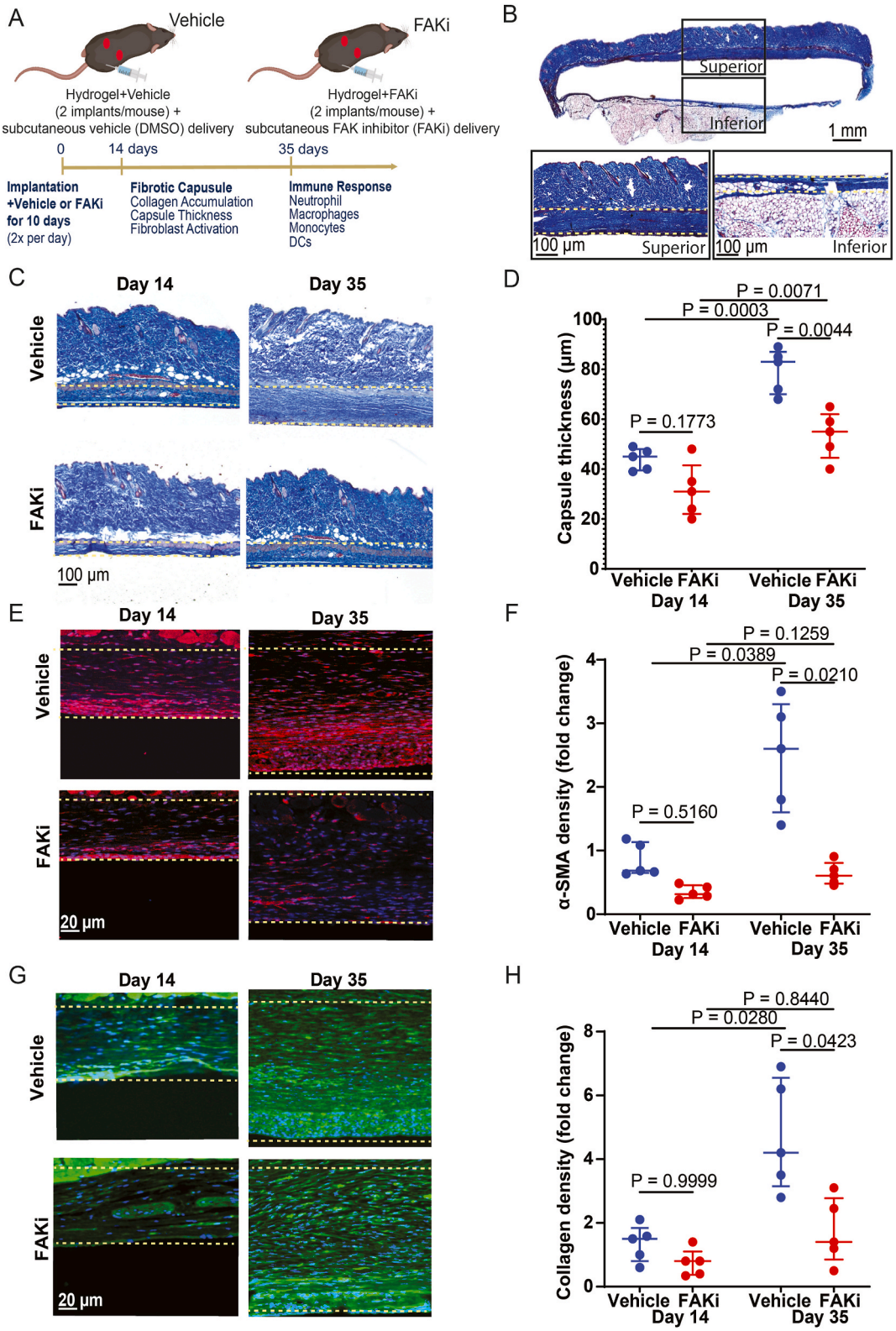

Fig. 2. FAK inhibition reduces fibrotic capsule formation, myofibroblast accumulation, and collagen deposition around stiff hydrogel. A) Experimental schematic. Mice received bilateral subcutaneous PEG-4aNB hydrogels on day 0. Beginning immediately post-implantation, animals were randomized to vehicle (DMSO) or FAKi (VS-6063). Injections were administered twice daily on days 0–10 adjacent to the implant site. Tissues were harvested on day 14 and day 35. **B**) Representative Masson's trichrome-stained section showing fibrotic capsule on superior and inferior facets of hydrogel. **C**) Masson's trichrome-stained sections from vehicle and FAKi groups at day 14 and day 35 showing differences in capsule thickness. **D**) Quantification of fibrotic capsule thickness at the hydrogel–tissue interface. FAKi significantly reduced capsule thickness on day 35. **E**) Immunofluorescence images for α-SMA (red) and nuclei (DAPI, blue). **F**) Quantification of $\alpha\text{-SMA}^{+}$ area reveals decreased myofibroblast accumulation in FAKi-treated mice. **G**) Collagen I immunofluorescence images (DAPI counterstain) and **H**) corresponding quantification. Data represent median ± IQR; Capsule thickness, and collagen I intensity data were analyzed by two-way ANOVA with Bonferroni's post hoc test. α-SMA intensity was analyzed by one way Welch's ANOVA.

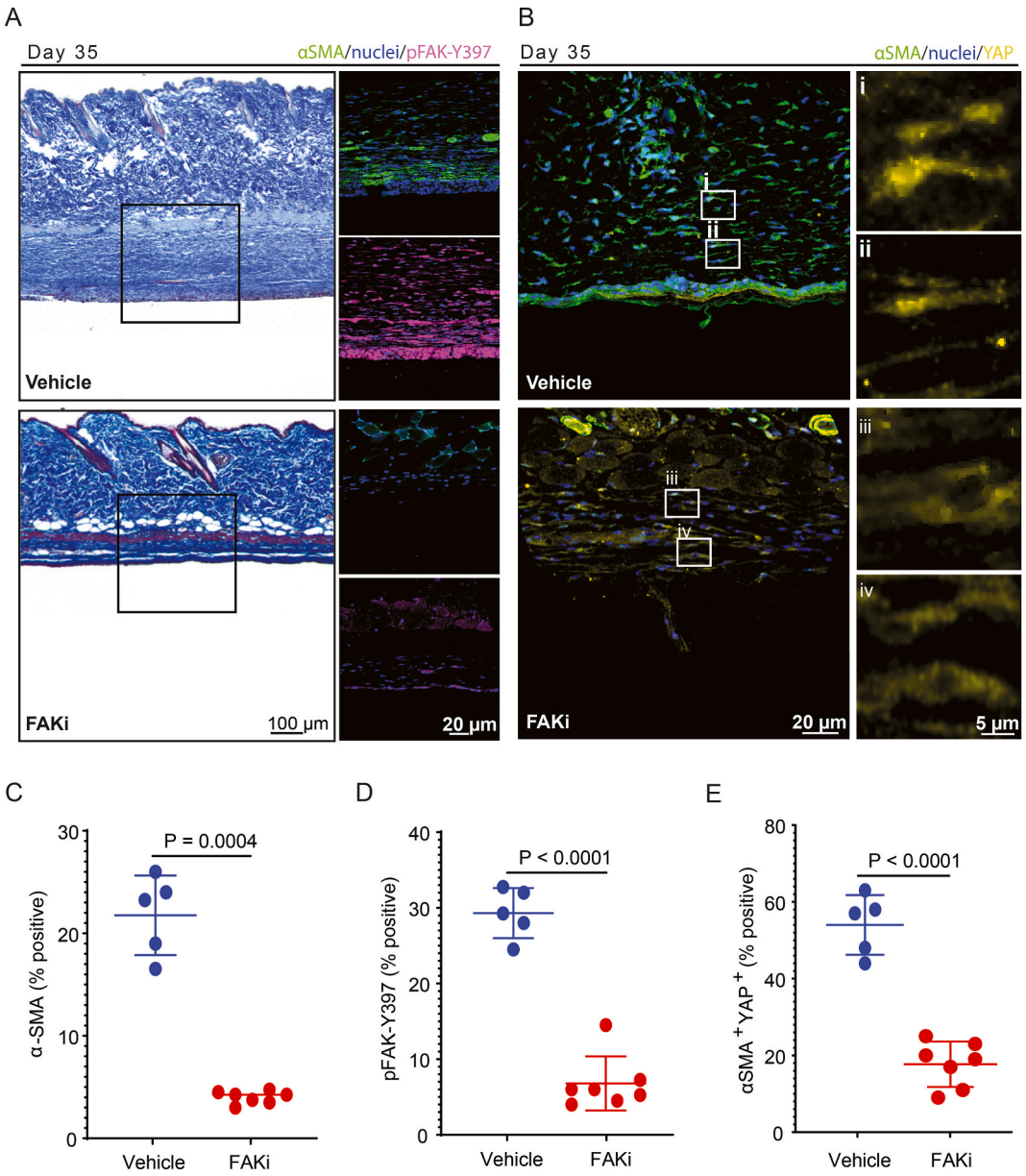

Fig. 3. FAKi suppresses focal adhesion signaling and YAP-mediated myofibroblast activation in stiff hydrogel fibrotic capsules. **A**) Masson's trichrome–stained sections and corresponding immunostained images of peri-implant fibrotic capsules surrounding stiff (12 kPa) hydrogels at day 35 post-implantation. Sections are stained for α-smooth muscle actin (α-SMA, green) and phosphorylated FAK at tyrosine-397 (pFAK-Y397, magenta) with nuclei counterstained with DAPI (blue). Boxed regions indicate areas shown at higher magnification. **B**) High-magnification confocal images illustrating YAP nuclear localization within α-SMA$^+$ regions of the fibrotic capsule. In vehicle-treated samples (i–ii), YAP signal is enriched within nuclei of α-SMA$^+$ cells. In FAKi-treated samples (iii–iv), YAP signal is diminished and less nuclear. **C**) Quantification of α-SMA$^+$ area within the fibrotic capsule, showing reduced myofibroblast activation under FAK inhibition ($P = 0.0004$). **D**) Quantification of pFAK-Y397$^+$ area expressed as a percentage of total capsule area. FAKi reduces FAK activation ($P < 0.0001$). **E**) Quantification of α-SMA$^+$ cells that were nuclear YAP$^+$, expressed as a percentage of total α-SMA$^+$ cells. Each dot represents one animal ($n = 5–7$ per group). Data are shown as mean ± SD. Statistical significance was assessed using unpaired two-tailed tests.

irrespective of treatment. Classical monocyte (Ly6C$^+$) numbers remained constant across both groups and timepoints (Fig. 5E), indicating that their recruitment at the tissue-biomaterial interface is independent of FAK activity.

The overall F4/80$^+$ macrophage population increased from day 14–35 in both control and FAKi groups (Fig. 5F), consistent with histological observations. Immunofluorescence staining for macrophage marker CD68 confirmed this trend, showing a time-dependent increase in macrophage density ($P = 0.0409$) in the fibrotic capsule of stiff hydrogels for vehicle-treated animals (Fig. S2). Notably, FAKi significantly suppressed macrophage accumulation, stabilizing macrophage numbers by day 35 ($P > 0.9999$), yielding a 46 % lower macrophage density compared to controls at day 35 ($P = 0.0322$). Whereas these data are correlative, they are consistent with prior work showing that FAK signaling promotes macrophage motility/chemotaxis and that FAK inhibition tempers local macrophage accumulation *in vivo* [32]. In addition, FAK activity can potentiate TNF-α–induced secretion of matrix-degrading enzymes (e.g., MMPs) and chemokines that support recruitment [32,33]. Although the total macrophage proportion remained unaffected by FAKi, subset-specific responses became evident upon deeper phenotypic analysis. Pro-inflammatory, M1-like macrophages (CD86$^+$CD206$^-$MHC-II^{hi}) increased over time in the FAKi group ($P = 0.0194$; Fig. 5G) but remained unchanged in controls. Conversely, M2c-like macrophages (CD86$^+$CD206$^+$CD163$^+$), typically linked to

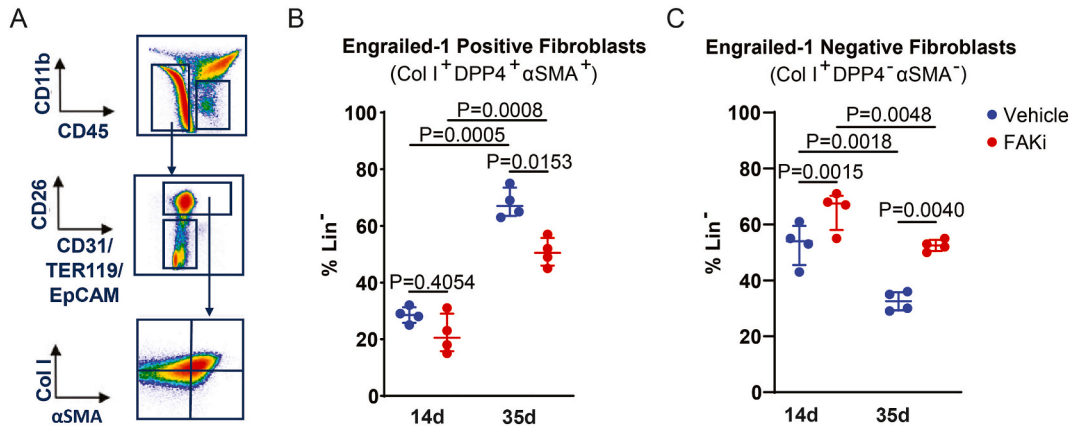

Fig. 4. FAK inhibition shifts fibroblast lineage composition. A) Spectral-flow gating distinguishes (Col I^+ $DPP4^+$ α-SMA^+ ($En1^+$ myofibroblast) and Col I^+ $DPP4^-$ α-SMA^- ($En1^-$ fibroblast) populations. **B**) $En1^+$ myofibroblasts were reduced nearly 30 % in FAKi-treated capsules at day 35. **C**) $En1^-$ fibroblasts increased to >70 % of $CD45^-$ stromal cells with FAKi. Data represent median ± IQR; Two-way ANOVA with Bonferroni's multiple comparisons test.

pro-fibrotic remodeling [34,35], were stable over time in controls but showed a decline at day 35 under FAKi (P = 0.0469; Fig. 5H), implicating FAK activity as a key regulator of macrophage polarization towards a fibrotic phenotype. Additionally, scaffold-associated macrophages ($F4/80^+CD11c^+$), a subset associated with biomaterial integration and fibrosis [30,31], accumulated in control capsules but were diminished by day 35 under FAKi (P = 0.0181; Fig. 5I), highlighting the critical role of FAK signaling in their recruitment, persistence, and in shaping local macrophage polarization at the tissue–biomaterial interface. Although the percentage of $CD86^+CD206^-MHC\text{-}II^{hi}$ (M1-like) macrophages increased modestly in FAKi-treated capsules, this occurred within an overall smaller macrophage compartment (CD68 IF, −46 % vs vehicle at day 35) and was not accompanied by elevations in IL-1β, TNF-α, IL-6, or IFN-γ (Fig. 6C; Fig. S4). In parallel, $CD86^+CD206^+CD163^+$ (M2c-like) macrophages and $F4/80^+CD11c^+$ scaffold-associated macrophages declined under FAKi, consistent with reduced α-SMA, collagen I, and capsule thickness. Although FAK signaling is implicated across multiple leukocyte lineages, in this biomaterial-induced fibrosis setting its effects appeared selective as neutrophils, dendritic cells, $CD8^+$ T cells, B cells, NK cells, and total $CD11c^+$ cells showed no significant differences between treatment groups or over time (Fig. S3). Together, these findings suggest that FAK activity sustains a pro-fibrotic immune niche enriched in M2c-like and scaffold-associated macrophages. In contrast, FAK inhibition selectively reprograms this environment by reducing pro-fibrotic subsets without enhancing pro-inflammatory responses. Pharmacological inhibition of FAK activity disrupts this axis, transiently enhancing anti-inflammatory monocyte presence and regulatory T cell abundance, diminishing immunological feedback mechanisms necessary for sustained fibrotic capsule formation.

To further characterize the inflammatory milieu underlying these immune shifts, we performed 32-plex cytokine profiling of fibrotic capsule lysates at day 35 using Luminex-based bead array (Fig. 6A, Fig. S4). Unsupervised hierarchical clustering of the cytokine profiles revealed distinct expression patterns between groups, with FAKi-treated samples clustering separately from vehicle controls (Fig. 6A). Principal component analysis similarly showed separation along PC1 (48.7 % of total variance), indicating a consistent shift in the overall cytokine profile with FAKi (Fig. 6B).

We next examined the most differentially expressed analytes (Fig. 6C). Relative to vehicle, FAK inhibition was associated with lower levels of G-CSF, MCP-1, VEGF, IL-6, IL-13, and IP-10, while IL-10 was increased. TNF-α and IFN-γ were not increased across the panel (Fig. 6A; Fig. S4). Across the cytokine panel, FAKi showed a selective suppression of pro-fibrotic and pro-remodeling mediators, rather than broad immune activation. Consistent with reduced fibrosis, FAKi decreased cytokines associated with fibroblast activation and chemotaxis (IL-6, IP-10), type 2 immune responses (IL-5, IL-13) and reduced angiogenic growth factor signals (VEGF, G-CSF) [28,36]. In addition, chemokines linked to leukocyte recruitment and foreign body remodeling, including MCP-1, were reduced under FAKi. Several l analytes lie close to the assay detection limit (dashed line, Fig. S4). Together, these data show that FAK inhibition altered the day-35 capsule cytokine milieu, with reductions in multiple cytokines/chemokines and growth factors alongside increased IL-10, without a corresponding increase in canonical type-1 inflammatory cytokines (IFN-γ, IL-17).

3. Discussion

Tissue repair and fibrosis emerge from the integration of mechanical cues with coordinated stromal and immune responses. While fibroblast heterogeneity and transcriptional states have been extensively characterized across a wide range of mechanical environments, less attention has been paid to how relatively modest, physiologically relevant differences in matrix stiffness shape these processes *in vivo*. We therefore focused on a moderate stiffness regime (4–12 kPa). Within this window, fibrotic capsule formation was highly sensitive to mechanical context. Stiff hydrogels (12 kPa) supported sustained fibroblast activation and capsule thickening, whereas soft matrices (4 kPa) elicited minimal remodeling, consistent with lower basal mechanical signaling. Pharmacological inhibition of FAK (FAKi) altered this response. Around stiff implants, FAK inhibition attenuated capsule thickness and reduced myofibroblast accumulation, while soft implants were largely unaffected by treatment. RGD adhesive peptide was included within the hydrogel as a chemically defined integrin-binding cue and its concentration was held constant across all implants; this design allowed us to isolate the contribution of hydrogel stiffness to FAK-dependent mechanotransduction and the peri-implant host response, rather than confounding comparisons by differences in adhesive ligand presentation.

At the stromal level, spectral flow cytometry revealed that FAKi selectively reduced α-$SMA^+Col\ I^+DPP4^+$ (En1-like) pro-fibrotic fibroblasts while increasing α-$SMA^-Col\ I^+DPP4^-$ fibroblasts, consistent with lineage-tracing studies implicating $DPP4^+En1^+$ fibroblasts in scar-forming myofibroblast programs [26]. Histological readouts showed robust pFAK-Y397 levels together enriched nuclear YAP localization in α-SMA^+ cells in vehicle-treated mice, whereas FAKi reduced pFAK-Y397 activation and reduced nuclear YAP localization within the α-SMA^+ compartment. Although these observations do not establish YAP/TAZ causality, they align with an overall reduction in focal adhesion-associated mechanical signaling in the capsule wall.

FAKi also reshaped the peri-implant immune niche. Pro-fibrotic scaffold-associated ($F4/80^+CD11c^+$) and M2c-like ($CD206^+CD163^+$)

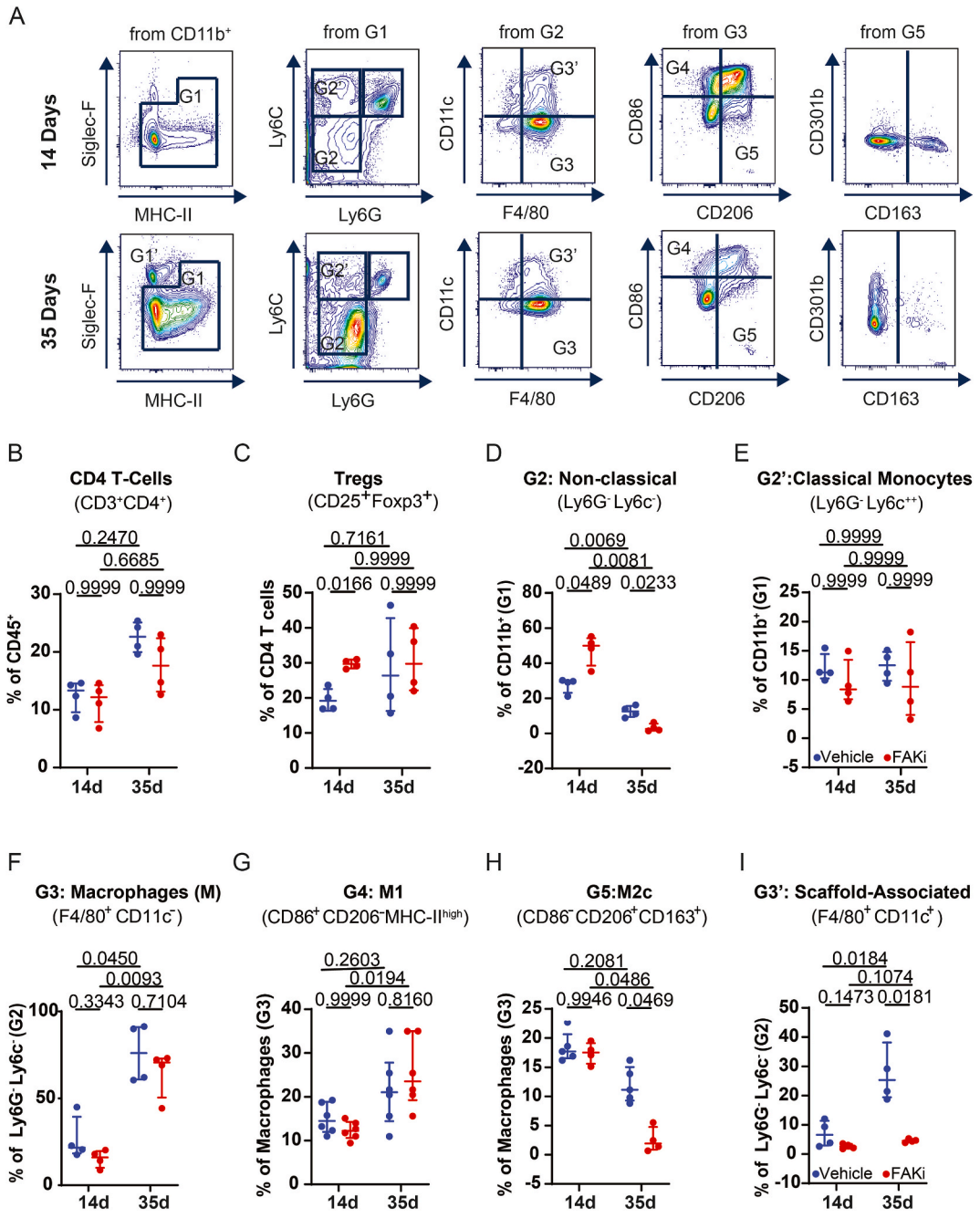

Fig. 5. FAK remodels the immune niche. A) Gating strategy for lymphoid and myeloid subsets at days 14 and 35 post-implantation. Quantification of immune cell populations, comparing vehicle (blue) and FAKi (red) groups for **B)** $CD4^+$ T cells, **C)** regulatory T cells ($CD25^+FoxP3^+$), **D)** $Ly6C^-$ non-classical monocytes ($Ly6C^-$), and **E)** $Ly6C^+$ classical monocytes. **F)** Total $F4/80^+CD11c^-$ macrophages, **G)** M1-like ($CD86^+CD206^-MHC\text{-}II^{hi}$) macrophages, **H)** M2c macrophages ($CD86^+CD206^+CD163^+$), and **I)** $F4/80^+CD11c^+$ scaffold-associated macrophages. Data represent median ± IQR. Statistical comparisons were performed using two-way ANOVA with Bonferroni's post hoc test, except for panels F–I, where normality assumptions were not met and Kruskal–Wallis test followed by Dunn's multiple comparisons test was applied.

macrophage subsets were reduced at day 35, while M1-like macrophages were modestly increased [34,35]. Cytokine profiling at day 35 showed decreased levels of IL-6, IL-13, VEGF and G-CSF, consistent with dampened type-2 signaling, angiogenesis support, and fibroblast activation [35,37]. Notably, IL-10 increased in the absence of IFN-γ or TNF-α induction, consistent with a compensatory immunoregulatory feedback rather than classical inflammatory activation. Tregs were initially elevated early under FAKi but were stabilized a later stage, providing a plausible route to IL-10 production, yet the primary source in the capsule remains to be established. FAKi has been reported to reduce Treg abundance in tumor settings through disruption of nuclear FAK-dependent CCL5 recruitment [18,20]. In our peri-implant fibrotic niche, however, RANTES/CCL5 values did not differ between groups. Total $CD4^+$ or $CD8^+$ T cell abundance or the CD4:CD8 were unchanged, suggesting that FAKi did not broadly alter the overall T cell compartment. Resolving whether the Treg signal reflects recruitment versus local maintenance will require lineage-resolved strategies.

In this framework, FAK functions as a mechanotransduction hub linking matrix stiffness to fibroblast contractility and cytokine outputs, with downstream consequences for immune networks at the biomaterial–tissue interface [38,39]. Integrin-mediated FAK activation promotes fibroblast survival, contractility, and matrix deposition. Our

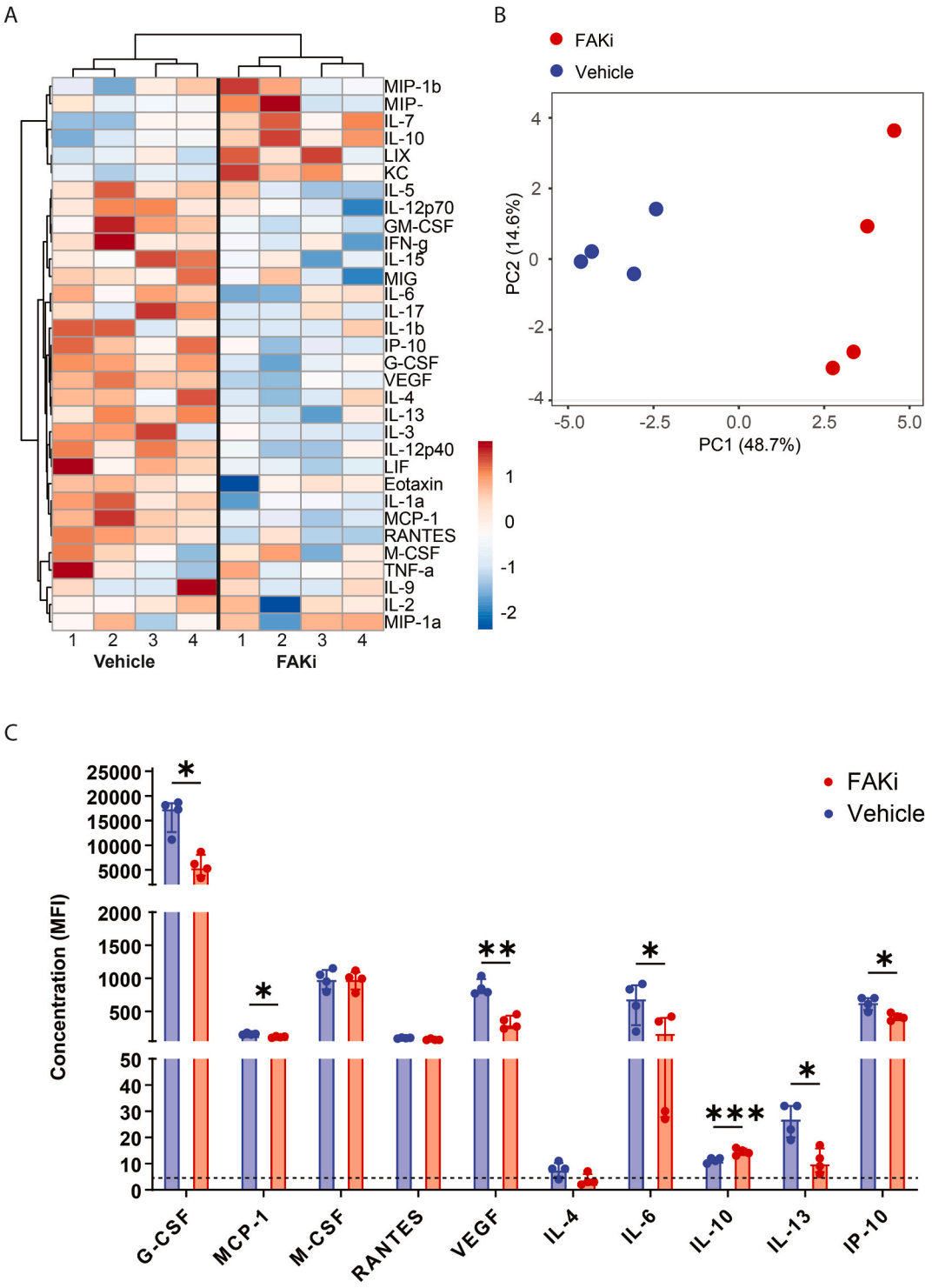

Fig. 6. FAK inhibition suppresses a pro-fibrotic cytokine network. A) Heatmap of z-scored cytokine concentrations (32-plex Luminex) from day-35 capsules; rows and columns clustered by Ward.D2. B) PCA of $\log_{10}$ concentrations shows clear separation along PC1 (48.7 % variance). C) Box plots of key cytokines reveal significant downregulation of IL-13, VEGF, GM-CSF, IL-6 and IP-10 with FAKi (median ± IQR, linear model with Tukey adjustment, *P < 0.05, **P < 0.01, ***P < 0.001).

data suggests that stiffness-dependent FAK activation also interfaces with additional mechanosensitive regulators. Reduced YAP nuclear localization in α-SMA^{+} cells under FAKi is consistent with disruption of myofibroblast-associated mechano-transcriptional programs. In parallel, mechanosensitive ion channels—particularly Piezo1—have been implicated upstream of YAP-dependent programs that promote myofibroblast differentiation. An important next step will be to dissect how FAK signaling interfaces with such mechano-ionic pathways *in vivo* [40–42].

By identifying a shared upstream regulator of both myofibroblast activation and immune suppression, our study provides a compelling rationale for FAK as a therapeutic target in implant fibrosis. Our strategy of local peri-implant injections of FAKi biased exposure toward the fibrotic niche while limiting systemic effects, and future strategies such

as hydrogel-tethered FAKi, release-on-demand conjugates, or mechano-responsive systems, could enhance precision and limit off-target effects. A limitation of the current approach is that repeated bolus injections may produce local concentration gradients over time. Future work will evaluate implant-integrated FAKi delivery (e.g., controlled release or tethering from the PEG network) to provide sustained, spatially confined inhibition at the tissue–implant interface.

This study has several additional limitations. First, we focused on a murine subcutaneous implantation model and a 35-day experimental window, which does not capture orthotopic tissue complexity or long-term remodeling. Second, cyclic mechanical loading would be required to reveal additional mechano-immune interactions. Third, pharmacological FAK inhibitors can exhibit off-target effects (including on PYK2), and genetic or cell-type–specific perturbations would strengthen causal inference [43]. In addition, prolonged studies will be needed to rule out late, low-grade inflammatory effects. Encouragingly, no overt toxicity or weight loss was observed during the injection regimen, but longer-term safety and implant-anchored delivery strategies remain to be explored. While our analysis emphasizes tissue-level remodeling, we have previously shown that fibroblast adhesion-mediated FAK activity and YAP nuclear localization is stiffness-dependent within the same range studied here [44,45]; and integrin-mediated mechanotransduction reshapes macrophage functions [17]. Building on this foundation, future *in vitro* assays such as traction force microscopy, calcium imaging, and single-cell FRET biosensors will be critical to dissect how FAK inhibition rewires mechanotransduction programs in both fibroblasts and immune populations.

4. Materials and methods

4.1. Hydrogel synthesis

PEG-4aNB macromer (2 kDa, custom-synthesized; Jenkem Technology) was used to generate synthetic hydrogels with tunable stiffness in the fibrotic range. Hydrogels were prepared at 6 % and 24 % (w/v) by dissolving PEG-4aNB in 10 mM HEPES-buffered PBS (pH 7.4). Thiol–ene crosslinking was initiated using 1.0 mM lithium phenyl-2,4,6-trimethylbenzoylphosphinate (LAP; Tocris) as the photoinitiator and stoichiometric amounts dithiothreitol (DTT; Sigma-Aldrich**)** as the crosslinker and RGD peptide (GRGDSPC, Vivitide) was added at 1.0 mM final concentration to provide adhesive cues.

For polymerization, 250 μL of the precursor solution was pipetted into custom cylindrical PDMS molds (10 mm diameter × 2 mm height) and exposed to UV light using an OmniCure S2000 UV system (Excellitas Technologies) at 85 ± 5 mW cm^{-2} for 10 s. Following crosslinking, hydrogels were rinsed in sterile PBS and equilibrated for 18 h at room temperature prior to implantation. Stiffness tuning was achieved by modulating the polymer weight percentage, with 6 %–24 % (w/v) PEG-4aNB hydrogels yielding a stiffness range from ~4 to 12 kPa, as confirmed by oscillatory shear rheometry.

4.2. Mechanical characterization

Rheological measurements were performed on an MCR 302 rheometer (Anton Paar) using a 2° cone with a 10 mm diameter plate. Storage (G′) and loss (G″) moduli were determined from an oscillatory frequency sweep (1–10 Hz) at 1.5 % strain, within the linear viscoelastic region as defined by preliminary amplitude sweeps. All measurements were conducted at 25 °C in hydrated conditions (n = 5).

4.3. Subcutaneous implantation

All animal procedures were performed with approval of the Georgia Tech Animal Care and Use Committee with veterinary supervision and within the guidelines of the Guide for the Care and Use of Laboratory Animals. The surgical procedure was adapted from published protocols [25,46]. Only C57BL/6J male mice (10–12 weeks old) were used for all experiments to avoid sex-related variability in immune responses. Mice were anesthetized with 2–3 % isoflurane in oxygen, and the dorsal surface was shaved and cleaned using alternating scrubs of 70 % ethanol and chlorhexidine. Post-operative analgesia was provided via subcutaneous injection of buprenorphine (0.1 mg/kg) every 12 h for 48 h.

Two subcutaneous dorsal pockets were created per animal via blunt dissection following ~10 mm longitudinal skin incisions made approximately 1 cm lateral to the spine, one on each side of the dorsum. Precast PEG-4aNB hydrogel disks (250 μL; 10 mm diameter × 2 mm thickness; 6 % or 24 % w/v, corresponding to ~4 kPa and ~12 kPa, respectively) were inserted into the pockets and positioned within the dorsal subcutaneous space superficial to the panniculus carnosus. To avoid inter-implant interactions, implants were placed in separate pockets on opposing sides of the dorsum. Skin incisions were closed using 6-0 nylon sutures (Ethicon), and animals were monitored daily for signs of distress, infection, or implant extrusion.

FAK inhibitor (FAKi) or vehicle was administered by subcutaneous injection into the dorsal flank, immediately adjacent (2–3 mm) to the implant pocket/skin incision and overlying the implant, as illustrated in Fig. 2A. Injections were placed ~1 cm lateral to the spine and delivered into the same subcutaneous plane as the implant to bias drug exposure toward the peri-implant tissue while minimizing systemic effects. To assess whether proximity to the injection site influenced outcomes, implants located ipsilateral versus contralateral to the injection site were compared, and no positional or side-of-body effects were detected for fibrotic capsule thickness, α-SMA expression, collagen I deposition, or macrophage density (all $P > 0.2$); therefore, data were pooled across sides.

To inhibit FAK kinase activity, mice received subcutaneous bolus injections of the ATP-competitive FAK/PYK2 inhibitor VS-6063 (defactinib; Selleckchem) at 15 μM in 150 μL per injection, administered twice daily for 10 days post-implantation. Control animals received matched injections of vehicle (20 % DMSO in sterile PBS) on the same schedule. Animals were monitored daily for body weight, grooming, posture, and injection-site reactions (erythema, induration, ulceration), and no overt toxicity or local adverse effects were observed.

At experimental endpoints (days 14 and 35 post-implantation), mice were euthanized by CO_2 asphyxiation followed by cervical dislocation. Implants with surrounding peri-implant tissue were excised en bloc and processed for histological analysis, flow cytometry, and cytokine profiling.

4.4. Histology, immunostaining, and image analysis

Hydrogels with surrounding subcutaneous tissue were excised and fixed in 10 % neutral-buffered formalin for 24 h at room temperature. Fixed tissues were dehydrated through an ethanol gradient, cleared in xylene, embedded in paraffin, and sectioned at 5 μm thickness. Sections were stained using hematoxylin and eosin (H&E) to assess cellular organization and general histology. For fibrosis assessment, Masson's trichrome staining was performed to visualize collagen deposition. Paraffin-embedded sections underwent heat-mediated antigen retrieval in 0.1 M citrate buffer (pH 6.0) at 95 °C for 15 min, followed by PBS-Tween washes. For fluorescence analysis, sections were blocked with 10 % goat serum. Sections were incubated overnight at 4 °C with antibodies against collagen I (Rockland 600-401-103-05; 1:100), α-SMA (mouse IgG2a, anti-SM1; 1:100), and CD68 (ab125212, Abcam; 1:100). Alexa Fluor 488- or 647-conjugated secondary antibodies (Invitrogen A-11034 and A-21241) were used for detection. Nuclei were counterstained with DAPI (Sigma D9542; 1:50). Images were acquired on Nikon Ti2-E motorized inverted microscope and AX-R confocal system, using a high magnification objective (× 40 CFI60 Apochromat Lambda S LWD 40× Water Immersion Objective Lens, N.A. 1.15, W.D. 0.59–0.61 mm, F.O.V. 22 mm, DIC, Correction Collar 0.15–0.19 mm). Images were exported as 12-bit tiff files and further analysis was performed using

ImageJ software. Fluorescent signal quantification was performed in regions of interest covering the fibrotic capsule and adjacent wound bed, and the positive area was expressed as a percentage of total tissue area. For α-SMA and pFAK-Y397, percentage of positive area was calculated as (thresholded positive pixels/total ROI pixels) × 100, using a single fixed threshold per marker applied to all images in the staining batch (set from background/negative controls). For YAP, nuclei were segmented from DAPI; a nucleus was scored YAP^+ if mean nuclear YAP intensity exceeded the same batch threshold, and percentage of YAP^+ was calculated as (YAP^+ nuclei/total nuclei) × 100. At least 5 ROIs per animal were averaged to yield one value per animal.

Capsule thickness and marker quantification.

For hydrogel implant analysis, fibrotic capsule thickness was measured from the implant interface to the panniculus carnosus. Quantitative analysis of α-SMA^+, $CD68^+$, and collagen I^+ areas was performed in at least three fields per section as a percentage of the positive staining in the entire capsule area using ImageJ. Measurements were blinded and averaged per animal. All representative images were contrast-adjusted identically across groups in Adobe Photoshop (CS4) for visualization purposes only. No image manipulations were performed for quantification.

4.5. Flow cytometry

Hydrogel samples were recovered without surrounding tissue, chopped and digested using dispase II and type II collagenase dissociation buffer (RPMI 1640, 2.5 U/mL Dispase II (ThermoFisher, 17105041), 0.2 % Type II Collagenase (Worthington Biochemical Corp., LS004176) at 37 °C for 1 h. The digested tissue suspension was then passed through a 35 μm cell strainer (Falcon, 352,235) and washed with 5 mL of PBS. Red blood cells were lysed using RBC Lysis Buffer (BioLegend, 420,301), and the cell pellet was rinsed first with FACS buffer (HBSS (ThermoFisher, 14175103), 2 mM EDTA (Invitrogen, AM9260G, 0.5 % bovine serum albumin (Sigma-Aldrich, A9418) then with PBS. Cells were first stained for surface markers in FACS buffer (HBSS, 2 mM EDTA, 0.5 % BSA) for 30 min at 4 °C, washed, then fixed and permeabilized for intracellular staining. Cells were fixed using Fixation Buffer (BioLegend, 420,801). Absolute cell counts were determined using Precision Count Beads (BioLegend, 424,902). For FoxP3, we used a transcription factor fix/perm kit (e.g., True-Nuclear™ Transcription Factor Buffer Set, BioLegend) following the manufacturer's protocol (fix 45 min, perm washes, anti-FoxP3 30–45 min in perm buffer). For stromal intracellular antigens (α-SMA, Col1a1), cells were fixed (Cytofix) and permeabilized (Cytoperm/perm wash) and stained 30 min at room temperature in perm buffer. All intracellular antibodies were validated for flow on fixed/permeabilized cells (clone, fluorophore, vendor, and dilution in Table S1). Fluorescence-minus-one (FMO) controls were run for FoxP3, α-SMA, Col1a1, CD163, and CD206; single-stained compensation beads were used for spectral unmixing. Viability was assessed with Fixable Blue Dead Cell Dye prior to fixation.

Data was collected using a Cytek Aurora spectral flow cytometer. Spectral unmixing used single-stained compensation beads (UltraComp eBeads for IgG-based antibodies; ArC amine-reactive beads for viability dye) acquired each run to build the unmixing matrix on the Aurora cytometer. A description of the gating hierarchy and marker combinations used to define each population is provided in Fig. S5. FMOs were included for FoxP3, α-SMA, Col1a1, CD163, CD206. No post-hoc compensation was applied beyond the instrument's unmixing; minor spillover adjustments (≤1 %) were verified against FMOs. FCS files were imported into FCSExpress (De Novo Software) and the CD45+CD11b + myeloid and CD45+CD11b-lymphoid population was identified using bivariate plots. The myeloid, lymphoid and stromal populations were then exported from FCSExpress and the number of cells were graphed using GraphPad Prism 9.

4.6. Cytokine profiling

Hydrogel-associated capsules were excised, weighed (20–40 mg), and snap-frozen in liquid N_2. For lysis, tissues were homogenized in ice-cold RIPA buffer (50 mM Tris-HCl pH 7.4, 150 mM NaCl, 1 % NP-40, 0.25 % Na-deoxycholate, 1 mM EDTA) supplemented with a 1 × complete EDTA-free protease-inhibitor cocktail (Thermo Fisher). Homogenates were sonicated on ice (3 × 5 s bursts, 20 % amplitude) and clarified by centrifugation (10,000×*g*, 10 min, 4 °C). Supernatants were aliquoted and stored at −80 °C. Total protein concentrations were determined by BCA (Thermo Fisher). Lysates were normalised to 0.5 mg mL^{-1} and analyzed in technical duplicate using the MILLIPLEX® MAP Mouse Cytokine/Chemokine 32-plex kit (MCYTMAG-70K-PX32, MilliporeSigma) on a MAGPIX® platform (Luminex). This assay directly quantifies cytokine protein concentrations from capsule lysates. Calibration and validation standards were run on each plate; intra-assay CVs were <10 % for all analytes. Median fluorescence intensity (MFI) values were converted to pg mL^{-1} using a 5-parameter logistic fit in xPONENT® 4.3. Values below the lower limit of detection (LLOD) were treated as left-censored; for downstream analyses and visualization, these values were replaced with LLOD/2. Analytes with values outside the quantifiable range in the majority of samples across all groups were excluded from downstream analyses and reported as below/above detection. Unsupervised hierarchical clustering (Ward's method, Euclidean distance) and principal component analysis (PCA with unit variance scaling and SVD-based imputation) were performed using ClustVis (https://biit.cs.ut.ee/clustvis/) [47].

4.7. Statistical analysis

All statistical analysis was performed using GraphPad Prism v9.5. Data are shown as mean ± SD for mechanical measurements and median ± interquartile range (IQR) for all biological data. All datasets were initially assessed for normality using the Shapiro–Wilk test and for homogeneity of variance using Levene's test. Depending on the outcome, either parametric or non-parametric statistical tests were selected. Figure legends specify the statistical tests used for each comparison, including two-way ANOVAs with Bonferroni's multiple comparisons test, Welch's ANOVA with Games–Howell post hoc for unequal variances, and Kruskal–Wallis with Dunn's test for non-parametric data. For cytokine datasets, log-transformed values were analyzed by one-way ANOVA with Tukey correction, and principal component analysis was used for multivariate clustering.

CRediT authorship contribution statement

Marc A. Fernández-Yagüe: Conceptualization, Data curation, Formal analysis, Funding acquisition, Methodology, Writing – original draft, Writing – review & editing. **Graham F. Barber:** Investigation. **Aránzazu del Campo:** Conceptualization, Funding acquisition, Writing – review & editing. **Andrés J. García:** Conceptualization, Formal analysis, Funding acquisition, Project administration, Writing – review & editing.

Declaration of competing interest

The authors declare no competing interests.

Acknowledgements

Research was funded by the U.S. National Institutes of Health (R01 EB024322, R01 HL175067) and the European Research Executive Agency under Individual GLOBAL Marie Skłodowska-Curie Actions Fellowship (Project No. 898737 —MECHANO FIBROSIS).

Appendix A. Supplementary data

Supplementary data to this article can be found online at https://doi.org/10.1016/j.biomaterials.2026.124010.

Data availability

The data will be available within the Article and its Supplementary Information. The authors will provide additional data as requested.

References

[1] T.D. Zaveri, J.S. Lewis, N.V. Dolgova, M.J. Clare-Salzler, B.G. Keselowsky, Integrin-directed modulation of macrophage responses to biomaterials, Biomaterials 35 (11) (2014) 3504–3515.

[2] N.E. Liang, M.F. Griffin, C.E. Berry, J.B. Parker, M.A. Downer, D.C. Wan, M. T. Longaker, Attenuating chronic fibrosis: decreasing foreign body response with acellular dermal matrix, Tissue Eng Part B Rev 29 (6) (2023) 671–680.

[3] E. Dondossola, B.M. Holzapfel, S. Alexander, S. Filippini, D.W. Hutmacher, P. Friedl, Examination of the foreign body response to biomaterials by nonlinear intravital microscopy, Nat. Biomed. Eng. 1 (2016) 7.

[4] M.F. Griffin, J.B. Parker, R. Tevlin, N.E. Liang, C. Valencia, A. Morgan, M. Kuhnert, M. Downer, E.L. Meany, J.L. Guo, D. Henn, R.S. Navarro, K. Shefren, D. Nguyen, G. C. Gurtner, S.C. Heilshorn, C.K.F. Chan, M. Januszyk, E.A. Appel, A. Momeni, D. C. Wan, M.T. Longaker, Osteopontin attenuates the foreign-body response to silicone implants, Nat. Biomed. Eng. 9 (2025) 1254–1275.

[5] J. Huang, T. Jiang, J. Qie, X. Cheng, Y. Wang, Y. Ye, Z. Yang, H. Yan, K. Yao, H. Han, Biologically inspired bioactive hydrogels for scarless corneal repair, Sci. Adv. 10 (51) (2024) eadt1643.

[6] X. Zhou, Z. Lu, W. Cao, Z. Zhu, Y. Chen, Y. Ni, Z. Liu, F. Jia, Y. Ye, H. Han, K. Yao, W. Liu, Y. Wang, J. Ji, P. Zhang, Immunocompatible elastomer with increased resistance to the foreign body response, Nat. Commun. 15 (1) (2024) 7526.

[7] B. Hinz, The myofibroblast: paradigm for a mechanically active cell, J. Biomech. 43 (1) (2010) 146–155.

[8] H. Yu, J.K. Mouw, V.M. Weaver, Forcing form and function: biomechanical regulation of tumor evolution, Trends Cell Biol. 21 (1) (2011) 47–56.

[9] S.K. Mitra, D.A. Hanson, D.D. Schlaepfer, Focal adhesion kinase: in command and control of cell motility, Nat. Rev. Mol. Cell Biol. 6 (1) (2005) 56–68.

[10] M.D. Schaller, Biochemical signals and biological responses elicited by the focal adhesion kinase, Biochim. Biophys. Acta 1540 (1) (2001) 1–21.

[11] I. Acebrón, R.D. Righetto, C. Schoenherr, S. de Buhr, P. Redondo, J. Culley, C. F. Rodríguez, C. Daday, N. Biyani, O. Llorca, A. Byron, M. Chami, F. Gräter, J. Boskovic, M.C. Frame, H. Stahlberg, D. Lietha, Structural basis of focal Adhesion kinase activation on lipid membranes, Embo J 39 (19) (2020) e104743.

[12] D. Lietha, X.M. Cai, D.F.J. Ceccarelli, Y.Q. Li, M.D. Schaller, M.J. Eck, Structural basis for the autoinhibition of focal adhesion kinase, Cell 129 (6) (2007) 1177–1187.

[13] H. Wang, A.S. Abhilash, C.S. Chen, R.G. Wells, V.B. Shenoy, Long-range force transmission in fibrous matrices enabled by tension-driven alignment of fibers, Biophys. J. 107 (11) (2014) 2592–2603.

[14] D.E. Discher, P. Janmey, Y.L. Wang, Tissue cells feel and respond to the stiffness of their substrate, Science 310 (5751) (2005) 1139–1143.

[15] J. Swift, I.L. Ivanovska, A. Buxboim, T. Harada, P.C. Dingal, J. Pinter, J. D. Pajerowski, K.R. Spinler, J.W. Shin, M. Tewari, F. Rehfeldt, D.W. Speicher, D. E. Discher, Nuclear lamin-A scales with tissue stiffness and enhances matrix-directed differentiation, Science 341 (6149) (2013) 1240104.

[16] D.W. Zhou, M.A. Fernández-Yagüe, E.N. Holland, A.F. García, N.S. Castro, E. B. O'Neill, J. Eyckmans, C.S. Chen, J. Fu, D.D. Schlaepfer, A.J. García, Force-FAK signaling coupling at individual focal adhesions coordinates mechanosensing and microtissue repair, Nat. Commun. 12 (1) (2021) 2359.

[17] M.A. Fernandez-Yague, L.A. Hymel, C.E. Olingy, C. McClain, M.E. Ogle, J. R. Garcia, D. Minshew, S. Vyshnya, H.S. Lim, P. Qiu, A.J. Garcia, E.A. Botchwey, Analyzing immune response to engineered hydrogels by hierarchical clustering of inflammatory cell subsets, Sci. Adv. 8 (8) (2022) eabd8056.

[18] A. Serrels, T. Lund, B. Serrels, A. Byron, R.C. McPherson, A. von Kriegsheim, L. Gomez-Cuadrado, M. Canel, M. Muir, J.E. Ring, E. Maniati, A.H. Sims, J. A. Pachter, V.G. Brunton, N. Gilbert, S.M. Anderton, R.J. Nibbs, M.C. Frame, Nuclear FAK controls chemokine transcription, Tregs, and evasion of anti-tumor immunity, Cell 163 (1) (2015) 160–173.

[19] K.A. Owen, F.J. Pixley, K.S. Thomas, M. Vicente-Manzanares, B.J. Ray, A. F. Horwitz, J.T. Parsons, H.E. Beggs, E.R. Stanley, A.H. Bouton, Regulation of lamellipodial persistence, adhesion turnover, and motility in macrophages by focal adhesion kinase, J. Cell Biol. 179 (6) (2007) 1275–1287.

[20] C.J. Rowe, U. Nwaolu, D. Salinas, J. Hong, J. Nunez, J.L. Lansford, C.F. McCarthy, B.K. Potter, B.H. Levi, T.A. Davis, Inhibition of focal adhesion kinase 2 results in a macrophage polarization shift to M2 which attenuates local and systemic inflammation and reduces heterotopic ossification after polysystem extremity trauma, Front. Immunol. 5 (14) (2023) 1280884.

[21] Y.H. Wei, Y.F. Wang, N.B. Liu, R. Qi, Y. Xu, K. Li, Y. Feng, B.M. Shi, A FAK inhibitor boosts Anti-PD1 immunotherapy in a hepatocellular Carcinoma mouse model, Front. Pharmacol. 12 (2022).

[22] F. Liu, J.D. Mih, B.S. Shea, A.T. Kho, A.S. Sharif, A.M. Tager, D.J. Tschumperlin, Feedback amplification of fibrosis through matrix stiffening and COX-2 suppression, J. Cell Biol. 190 (4) (2010) 693–706.

[23] J.J. Tomasek, G. Gabbiani, B. Hinz, C. Chaponnier, R.A. Brown, Myofibroblasts and mechano-regulation of connective tissue remodelling, Nat. Rev. Mol. Cell Biol. 3 (5) (2002) 349–363.

[24] B.D. Fairbanks, M.P. Schwartz, A.E. Halevi, C.R. Nuttelman, C.N. Bowman, K. S. Anseth, A Versatile synthetic extracellular Matrix mimic via Thiol-norbornene photopolymerization, Adv. Mater. 21 (48) (2009) 5005–5010.

[25] N. Noskovicova, R. Schuster, S. van Putten, M. Ezzo, A. Koehler, S. Boo, N. M. Coelho, D. Griggs, P. Ruminski, C.A. McCulloch, B. Hinz, Suppression of the fibrotic encapsulation of silicone implants by inhibiting the mechanical activation of pro-fibrotic TGF-beta, Nat. Biomed. Eng. 5 (12) (2021) 1437–1456.

[26] S. Mascharak, H.E. DesJardins-Park, M.F. Davitt, M. Griffin, M.R. Borrelli, A. L. Moore, K. Chen, B. Duoto, M. Chinta, D.S. Foster, A.H. Shen, M. Januszyk, S. H. Kwon, G. Wernig, D.C. Wan, H.P. Lorenz, G.C. Gurtner, M.T. Longaker, Preventing Engrailed-1 activation in fibroblasts yields wound regeneration without scarring, Science 372 (6540) (2021) eaba2374.

[27] T.A. Wynn, K.M. Vannella, Macrophages in tissue repair, regeneration, and fibrosis, Immunity 44 (3) (2016) 450–462.

[28] N.M. Chapman, J.C. Houtman, Functions of the FAK family kinases in T cells: beyond actin cytoskeletal rearrangement, Immunol. Res. 59 (1–3) (2014) 23–34.

[29] H. Jiang, S. Hegde, B.L. Knolhoff, Y. Zhu, J.M. Herndon, M.A. Meyer, T. M. Nywening, W.G. Hawkins, I.M. Shapiro, D.T. Weaver, J.A. Pachter, A. Wang-Gillam, D.G. DeNardo, Targeting focal adhesion kinase renders pancreatic cancers responsive to checkpoint immunotherapy, Nat Med 22 (8) (2016) 851–860.

[30] K. Sadtler, B.W. Allen, K. Estrellas, F. Housseau, D.M. Pardoll, J.H. Elisseeff, The scaffold immune microenvironment: Biomaterial-Mediated immune polarization in traumatic and nontraumatic Applications<sup/>, Tissue Eng Part A 23 (19–20) (2017) 1044–1053.

[31] C. Cherry, J.I. Andorko, K. Krishnan, J.C. Mejias, H.H. Nguyen, K.B. Stivers, E. F. Gray-Gaillard, A. Ruta, J. Han, N. Hamada, M. Hamada, I. Sturmlechner, S. Trewartha, J.H. Michel, L. Davenport Huyer, M.T. Wolf, A.J. Tam, A.N. Pena, S. Keerthivasan, C.J. Le Saux, E.J. Fertig, D.J. Baker, F. Housseau, J.M. van Deursen, D.M. Pardoll, J.H. Elisseeff, Transfer learning in a biomaterial fibrosis model identifies in vivo senescence heterogeneity and contributions to vascularization and matrix production across species and diverse pathologies, GeroScience 45 (4) (2023) 2559–2587.

[32] M.Y. Abshire, K.S. Thomas, K.A. Owen, A.H. Bouton, Macrophage motility requires distinct alpha5beta1/FAK and alpha4beta1/paxillin signaling events, J. Leukoc. Biol. 89 (2) (2011) 251–257.

[33] T. Harada, K. Yoshimura, O. Yamashita, K. Ueda, N. Morikage, Y. Sawada, K. Hamano, Focal adhesion kinase promotes the progression of aortic aneurysm by modulating macrophage behavior, Arterioscler. Thromb. Vasc. Biol. 37 (1) (2017) 156–165.

[34] K.E. Martin, A.J. Garcia, Macrophage phenotypes in tissue repair and the foreign body response: implications for biomaterial-based regenerative medicine strategies, Acta Biomater. 133 (2021) 4–16.

[35] C.E. Witherel, D. Abebayehu, T.H. Barker, K.L. Spiller, Macrophage and fibroblast interactions in biomaterial-mediated fibrosis, Adv Healthc Mater 8 (4) (2019) e1801451.

[36] A. Bhattacharyya, K. Boostanpour, M. Bouzidi, L. Magee, T.Y. Chen, R. Wolters, P. Torre, S.K. Pillai, M. Bhattacharya, IL10 trains macrophage profibrotic function after lung injury, Am. J. Physiol. Lung Cell. Mol. Physiol. 322 (3) (2022) L495–L502.

[37] Q. Wang, Z. He, M. Huang, T. Liu, Y. Wang, H. Xu, H. Duan, P. Ma, L. Zhang, S. S. Zamvil, J. Hidalgo, Z. Zhang, D.M. O'Rourke, N. Dahmane, S. Brem, Y. Mou, Y. Gong, Y. Fan, Vascular niche IL-6 induces alternative macrophage activation in glioblastoma through HIF-2alpha, Nat. Commun. 9 (1) (2018) 559.

[38] S.K. Mitra, S.T. Lim, A. Chi, D.D. Schlaepfer, Intrinsic focal adhesion kinase activity controls orthotopic breast carcinoma metastasis via the regulation of urokinase plasminogen activator expression in a syngeneic tumor model, Oncogene 25 (32) (2006) 4429–4440.

[39] P.W. Oakes, Y. Beckham, J. Stricker, M.L. Gardel, Tension is required but not sufficient for focal adhesion maturation without a stress fiber template, J. Cell Biol. 196 (3) (2012) 363–374.

[40] Y. Fu, P. Wan, J. Zhang, X. Li, J. Xing, Y. Zou, K. Wang, H. Peng, Q. Zhu, L. Cao, X. Zhai, Targeting mechanosensitive Piezo1 alleviated renal fibrosis through p38MAPK-YAP pathway, Front. Cell Dev. Biol. 9 (2021) 741060.

[41] L. Niu, B. Cheng, G. Huang, K. Nan, S. Han, H. Ren, N. Liu, Y. Li, G.M. Genin, F. Xu, A positive mechanobiological feedback loop controls bistable switching of cardiac fibroblast phenotype, Cell Discov 8 (1) (2022) 84.

[42] J. He, X. Cheng, B. Fang, S. Shan, Q. Li, Mechanical stiffness promotes skin fibrosis via Piezo1-Wnt2/Wnt11-CCL24 positive feedback loop, Cell Death Dis. 15 (1) (2024) 84.

[43] J.K. Slack-Davis, K.H. Martin, R.W. Tilghman, M. Iwanicki, E.J. Ung, C. Autry, M. J. Luzzio, B. Cooper, J.C. Kath, W.G. Roberts, J.T. Parsons, Cellular characterization of a novel focal adhesion kinase inhibitor, J. Biol. Chem. 282 (20) (2007) 14845–14852.

[44] E.N. Holland, M.A. Fernández-Yagüe, D.W. Zhou, E.B.O. Neill, A.U. Woodfolk, A. Mora-Boza, J.P. Fu, D.D. Schlaepfer, A.J. García, FAK, vinculin, and talin control mechanosensitive YAP nuclear localization, Biomaterials 308 (2024) 122542.

[45] D.W. Zhou, M.A. Fernandez-Yague, E.N. Holland, A.F. Garcia, N.S. Castro, E. B. O'Neill, J. Eyckmans, C.S. Chen, J. Fu, D.D. Schlaepfer, A.J. Garcia, Force-FAK

signaling coupling at individual focal adhesions coordinates mechanosensing and microtissue repair, Nat. Commun. 12 (1) (2021) 2359.
[46] L. Dunn, H.C. Prosser, J.T. Tan, L.Z. Vanags, M.K. Ng, C.A. Bursill, Murine model of wound healing, J. Vis. Exp. 75 (2013) e50265.
[47] T. Metsalu, J. Vilo, ClustVis: a web tool for visualizing clustering of multivariate data using Principal component Analysis and heatmap, Nucleic Acids Res. 43 (2015) W566–W570.